Journal of Applied Fluid Mechanics, Vol. 17, No. 3, pp. 559-570, 2024.
Available online at www.jafmonline.net, ISSN 1735-3572, EISSN 1735-3645.
https://doi.org/10.47176/jafm.17.3.2226

Erosion Characteristics and Flashing Flow of High-differential-pressure Control Valves: A Numerical Study using an Erosion-Coupled Dynamic Mesh

G. F. Ou[1], C. G. Wang[1] and H. Z. Jin[2, 3†]

[1] *School of Mechanical Engineering & Rail Transit, Changzhou University, Changzhou, Jiangsu, 213000, China*
[2] *Key Laboratory of Fluid Transmission Technology of Zhejiang Province, Zhejiang Sci-Tech University, Hangzhou, 310018, China*
[3] *National Safety Engineering Technology Research Center for Pressure Vessels and Pipeline, Hefei General Machinery Research Institute, Hefei 230031, China*

†*Corresponding Author Email: haozhejin@zstu.edu.cn*

ABSTRACT

To address the issue of erosion in the control valves of blackwater flash systems in the coal chemical industry, this study investigates the dynamic erosion characteristics of one such control valve. Computational fluid dynamics is employed to compare the results obtained with a static mesh and an erosion-coupled dynamic mesh, and the valve erosion is investigated by analyzing the erosion rate, the particle impact velocity, trajectories and angle. Moreover, the relationship between the deformation caused by erosion and the dispersion of the flash vapor phase in the valve is studied, focusing on the flow resistance coefficient. The results indicate that over a period of 9×10^6 s, the impact velocity and subsequent collisions of particles reduce, and the impact angle decreases with the accumulated deformation of the valve core. Notably, the valve core is influenced primarily by the cutting that results from low impact angles, leading to a substantial decrease in the overall erosion rate of the valve, amounting to a reduction of 56.4%. The region facing the flow is at significant risk of erosion, and as the opening decreases, the erosion zone extends gradually to the annular region of the valve core and valve head, leading to increased erosion deformation. Furthermore, as the flow resistance coefficient decreases, so does the vapor volume fraction inside the valve. This study provides a theoretical basis for predicting faults and developing online monitoring solutions for high-differential-pressure control valves in blackwater flashing systems.

Article History

Received August 14, 2023
Revised October 13, 2023
Accepted November 9, 2023
Available online January 1, 2024

Keywords:

Computational fluid dynamics
Control valve
Erosion
Erosion-coupled dynamic mesh
Flashing

1. INTRODUCTION

The processing equipment used in the coal chemical industry is frequently exposed to complex multiphase flows in which a solid-containing medium repeatedly scours the surfaces of equipment and pipelines, thereby giving rise to erosion as a significant concern. Of particular importance in coal chemical systems are blackwater control valves, which are prime locations for erosion failure. Prolonged exposure to high differential pressure and flow rate leads to severe deformation of the valve core and to flash evaporation of the contained medium, and thus the overall lifespan of these valves is a mere four to six months (Ou et al., 2019). Therefore, it is imperative to research control valves extensively to uncover their failure mechanisms.

As indispensable equipment for industrial production, valves have been subjected to many studies to solve the problem of valve erosion. Liu et al. (2023) conducted visual experiments to inspect the transient erosion process in a proportional valve; the results indicated the presence of “edge collapse” within the valve, with groove formation, spalling, and indentation identified as the underlying mechanisms, and it was observed that the viscosity of the medium and the concentration of particles contributed to an increased rate of spalling. Peng et al. (2021) used experimental and numerical simulation techniques to explore the gas–solid multiphase flow of the ball valve; it was found that the worn surfaces were influenced by multiple mechanisms, and a region of reduced flow velocity—commonly referred to as a stagnation zone—was observed in the sample center, with the erosion rate (ER) increasing with increasing impact

NOMENCLATURE			
CFD	Computational fluid dynamics	α_v	vapor volume fraction
ER	Erosion Rate	Δx_{face}	mesh deformation of a single face
ECDM	Erosion-coupled dynamic mesh	ξ	flow resistance coefficient
UDF	User-Defined Function	Δt_{MM}	time step of the mesh motion

angle and peaking at 30°. Li et al. (2022) studied the correlation between particle collision and failure morphology of a valve port, considering various factors; the findings revealed a significant association between the cone-angle within the valve and the service life of the valve, and gray correlation analysis was used to identify the three factors with the most impact on the valve, i.e., the pressure drop, the grain size, and the valve diameter. Liu et al. (2021b) conducted particle motion visualization experiments to discuss the particle movement characteristics of the valve. The findings indicate the presence of four distinct motion modes exhibited by the particles, namely displacement and rotate along the wall, displacement and rotation along the wall opposite to the flow, motion propelled by the fluid, and particle spinning within a vortex. The researchers have extensively explored the erosion failure morphology and influencing factors of valves, dedicating substantial efforts towards improving valve longevity. However, there is limited research on erosion failure in control valves specifically under high-pressure differentials and flash evaporation conditions.

Computational fluid dynamics (CFD) is an established technology for fluid analysis and predicting particle erosion on surfaces (Koca, 2022). By using predictive analysis, enterprises can implement effective measures to mitigate failure issues and minimize economic losses (Alnak et al., 2022). Numerous scholars have conducted extensive research on valves using CFD. Hu et al. (2022) research the erosion properties of a check valve by CFD; the findings indicated that the bottom of the valve core's sealing surface experiences the most extreme erosion damage, and the damage increases with increasing angle of the sealing surface. Zhao et al. (2023) conducted a thorough simulation analysis of the energy loss in a valve's cavitation flow, using CFD to optimize the valve structure and obtaining remarkable results; it was discovered that using a valve sleeve with a V-groove configuration reduced the overall entropy production by an impressive 7.46%, thereby greatly enhancing the valve's service life.

The aforementioned scholars analyzed the flow behavior in valves using CFD based on a static grid, but with advancements in CFD technology, there have also been studies that used dynamic mesh techniques to solve the problem of material deformation. For instance, Nguyen et al. (2014) investigated the interplay between material surface deformation and multiphase flow characteristics, revealing that erosion-induced alterations in surface profile can significantly impact the erosion mechanism. Parsi et al. (2019) studied the erosion characteristics of an experimental jet process by coupled-erosion-solver with a dynamic grid; it was found that as a pit on the surface of the sample deepened, the ER decreased. López et al. (2018) used an erosion-coupled dynamic mesh (ECDM) to predict the failure of the volute of a centrifugal pulp pump; high similarity was found with the actual failure situation, showing the applicability of this method for calculating the performance attenuation of the pump when it was eroded.

Currently, the ECDM method is used predominantly to examine jet and elbow phenomena, but its use for valves is comparatively limited. In the present investigation, CFD in conjunction with ECDM technology is used to forecast the behavior of a blackwater control valve. Comparison shows that using a dynamic mesh is better for simulating real-world failure scenarios and exhibits superior performance in erosion prediction. The erosion characteristics are investigated at various time intervals and with different orifice sizes, with ER, particle velocity, trajectories and angle as the primary parameters. Then, based on the erosion deformation of the valve core, the flashing in the valve is studied. The present findings provide valuable insights for predicting the failure of blackwater flash control valves and devising effective on-line monitoring strategies.

2. NUMERICAL MODEL

The finite-volume and Euler–Lagrange methods were used to emulate the internal erosion process of the blackwater control valve. The valve constitutes a vapor–liquid–solid three-phase flow problem, with the vapor–liquid phase considered as a continuous phase and the dilute solid phase described by the discrete phase model. The impact of vapor compressibility was not considered, and a user-defined function (UDF) was used for the vapor–liquid mass transfer. The ER was calculated using the Oka erosion model, while the surface deformation of the valve spool was determined using an ECDM.

2.1 Governing Equations

The mass-conservation and momentum-conservation equations of the fluid are as follows (Koca & Zabun, 2021):

$$\frac{\partial}{\partial t}(\rho)+\nabla\cdot\left(\rho\vec{v}\right)=0\,, \tag{1}$$

$$\frac{\partial}{\partial t}\left(\rho\vec{v}\right)+\nabla\cdot\left(\rho\vec{v}\vec{v}\right)=-\nabla p+\nabla\cdot(\bar{\bar{\tau}})+\rho\vec{g}+\vec{F}\,, \tag{2}$$

where $\vec{F}$ is the external force and the source term, p is the static pressure, ρ is the fluid density, and $\bar{\bar{\tau}}$ is the stress tensor.

The realizable model has been greatly improved compared with the standard model when calculating strong streamline bending and vortex, so the realizable

turbulence model is adopted. In order to save computing resources and improve the convergence of calculation, the Enhanced Wall Treatment method is adopted. (ANSYS, 2020).

2.2 Phase Change Model

Flash boiling is when saturated water becomes partially saturated water vapor because of the decreased pressure after high-pressure saturated water enters a low-pressure container. Its generation principle is similar to that of cavitation, with both being pressure-driven evaporation accompanied by vapor–liquid phase transition (Jin et al., 2017). In this study, according to the cavitation model and the relationship between pressure and saturation temperature, a UDF was used for the vapor–liquid mass transfer in the valve. The Zwart–Gerber–Belamri cavitation model (Zwart et al., 2004) is as follows:

$$\frac{\partial(\rho_v \alpha_v)}{\partial t}+\frac{\partial(\rho_v \alpha_v u_j)}{\partial x_j}=R_e-R_c\,, \tag{3}$$

where R_e is the vapor evaporation rate, R_c is the vapor generation rate, u_j is the cartesian velocity component, and ρ_v is the density.

As the vapor volume fraction increases, the nucleation density decreases, and α_v vapor volume fraction can be replaced. In its final forms, the equation can be rewritten as

$$R_e=F_v\frac{3\alpha_{\text{nuc}}(1-\alpha_v)\rho_v}{R_B}\sqrt{\frac{2}{3}\frac{P_v-P}{\rho_l}} \tag{4}$$

for evaporation and

$$R_c=F_c\frac{3\alpha_v\rho_v}{R_B}\sqrt{\frac{2}{3}\frac{P-P_v}{\rho_l}} \tag{5}$$

for condensation, where the volume fraction of nucleation sites is taken as $\alpha_{nuc}=5\times10^{-4}$, the bubble radius is taken as $R_B=10^{-6}$, the evaporation ratio is taken as $F_v=50$, and the condensation ratio is taken as $F_c=0.01$. The saturated vapor pressure of the liquid is defined by the Antoine equation (Thomson, 1946):

$$\log P_v=A-B/(t+C)\,, \tag{6}$$

Where P_v is the saturated vapor pressure of the liquid corresponding to temperature t, and A, B, and C are physical constants (A = 7.074, B = 1657.46, C = 227.02).

2.3 Discrete Solid Particle Phase

The multiphase flow is processed using the Euler-Lagrange method. The Navier–Stokes equation was employed to solve for the vapor–liquid two-phase flow, and the solid particles were considered as discrete phases. By calculating the momentum, energy, and mass transfer between the discrete phase and the fluid, the particle motion state was obtained. For the trajectories of the rigid particles, the linear momentum equations are

$$\frac{d_{X_p}}{dt}=u_p\,, \tag{7}$$

$$m_p\frac{d\vec{u}_p}{dt}=m_p\frac{\vec{u}-\vec{u}_p}{\tau_r}+m_p\frac{\vec{g}(\rho_p-\rho)}{\rho_p}+\vec{F}\,, \tag{8}$$

where m_p is the particle mass, $\vec{u}$ is the fluid phase velocity, $\vec{u}_p$ is the particle velocity, and $\vec{F}$ is the virtual mass force, pressure gradient force, and Saffman lift. Because the particle density is greater than the fluid density, the virtual mass force and pressure gradient force are significantly smaller than the drag force and so were not considered in this study (López et al., 2018). The Saffman lift effect is applicable for smaller particles and can be ignored because it does not significantly alter the particle flow (Duarte et al., 2017). The particle relaxation time τ_r is given by

$$\tau_r=\frac{\rho_p d_p^{\,2}}{18\mu}\frac{24}{C_d\,\text{Re}_p}\,, \tag{9}$$

where μ is the viscosity, d_p is the particle size, and Re_p is the relative Reynolds number:

$$\text{Re}_p\equiv\frac{\rho d_p\left|\vec{u}_p-\vec{u}\right|}{\mu}. \tag{10}$$

As obtained by Morsi and Alexander (2006), the drag coefficient is

$$C_d=a_1+\frac{a_2}{\text{Re}_p}+\frac{a_3}{\text{Re}_p^{\,2}}\,, \tag{11}$$

where a_1, a_2, and a_3 are associated with the relative Reynolds number as show in Table 1.

2.4 Erosion Model

Erosion is influenced by various factors, including the physical properties of particles, the mechanical properties of materials, impact angle and velocity, and ambient temperature. Based on experimental analysis, the erosion model given by Oka et al. (2005) takes various factors into account and is one of the most comprehensive (Liu et al., 2021a). So that, the Oka erosion model was used in this study and is expressed as

$$E(\gamma)=g(\gamma)E_{90}\,. \tag{12}$$

Here, $g(\gamma)$ is a function of the impact angle and E_{90} is the ER at the impact angle of 90°, expressed as

$$g(\gamma)=(\sin\gamma)^{n1}(1+H_v(1-\sin\gamma))^{n2}\,, \tag{13}$$

$$E_{90}=10^{-9}\rho K(aH_v)^{bk1}(V_p/V^*)^n(D_p/D^*)^{k3}\,, \tag{14}$$

where n_1, n_2, and n determined by the hardness of the target material and are given by

$$n_1=0.71(H_v)^{0.14}\,, \tag{15}$$

$$n_2=2.4(H_v)^{-0.94}\,, \tag{16}$$

$$n=2.3(H_v)^{0.038} \tag{17}$$

Table 1 Drag coefficients

Range	a_1	a_2	a_3
$10000 < \mathrm{Re}_p < 50000$	0.5191	−1662.5	5.4167×10^6
$5000 < \mathrm{Re}_p < 10000$	0.46	−490.546	5.787×10^5
$1000 < \mathrm{Re}_p < 5000$	0.357	148.62	-4.75×10^4

The term H_v is the Vickers hardness of the material, this study takes H_v = 1.83 GPa. In Eq. (14), we have ρ = 7990 kg/m^3, and $K(aH_v)^{bk1}$ is determined by the nature of the erosion and the particles causing it and herein is $65(H_V)^{-0.12}$. The term k_3 is determined by the type of particles used; we used SiO_2 particles and hence $k_3 = 0.19$. The term V^* is the reference velocity, which herein is V^* = 104 m/s. The term D^* is the reference diameter, which herein is D^* = 326 μm. Finally, V_p is the particle velocity. D_p is the particle size.

Energy is lost during particle–metal collisions, so the reflection velocity is lower than the incident velocity; therefore, the normal recovery coefficient and the tangential recovery coefficient are usually used to describe these collisions. We used the wall rebound model proposed by Forder et al. (1998) and expressed as

$$\begin{aligned} e_N &= 0.988 - 0.78\theta + 0.19\theta^2 - 0.024\theta^3 + 0.027\theta^4 \\ e_T &= 1 - 0.78\theta + 0.84\theta^2 - 0.21\theta^3 + 0.028\theta^4 - 0.022\theta^5 \end{aligned} \tag{18}$$

2.5 Erosion-Coupled Dynamic Mesh

To predict accurately the failure process within the valve, it is essential to consider the deformation caused by erosion of the valve core, and this can be achieved via the ECDM method (ANSYS, 2020). During the solution process, both the fluid and particle erosion are treated as being in the steady state, and the mesh evolves with the physical time step. In ANSYS Fluent, the mesh deformation for individual surfaces is calculated as

$$\Delta x_{face} = ER_{face} \frac{\Delta t_{MM}}{\rho_{wm}}, \tag{19}$$

where ER_{face} is the ER of the surface, Δt_{MM} is the time step of the mesh motion, and ρ_{wm} is the density of the wall material.

3. DESCRIPTION OF VALVE AND METHOD

3.1 Process Parameters

The coal chemical blackwater system involves a three-stage flashing process, consisting of medium flashing, low flashing, and vacuum flashing. The solid-laden blackwater from the gasification quenching furnace undergoes flashing and cooling before entering the flash tanks. Angle valves are installed in front of the flash tanks to control the liquid level and pressure between different tanks. These angle control valves are subjected to harsh conditions of high temperature, high different pressure, and dense particle concentration. Consequently, various failure issues are inevitable, making it crucial to understand the erosion characteristics of the angle valves in the blackwater system. This study was focused on angle valve LV-0301A located before the low-pressure flash tank. It operates at an inlet pressure of 0.6 MPa, an outlet pressure of 0.26 MPa, and a working temperature of 145°C. The parameters of the fluid medium are show in Table 2.

Table 2 Parameters of fluid medium for blackwater angle valve LV-0301A

	Liquid phase	Vapor phase	Solid phase
Density [kg·m^{-3}]	919	3.5	2320
Viscosity [kg·m^{-1}·s^{-1}]	1.85e-4	1.45e-5	\
Average particle size [μm]	\	\	150
Solid volume fraction [%]	\	\	<12
Saturated vapor pressure [kPa]	415.6	\	\

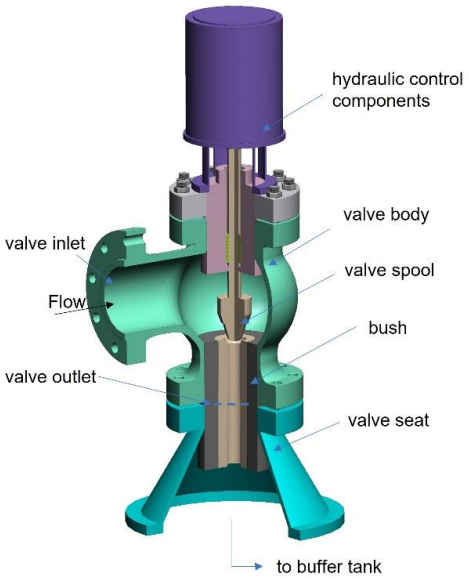

Fig. 1 Basic structure of valve

3.2 Model Description

Figure 1 shows the geometric structure of the blackwater angle valve, including the valve body, valve spool, bush, valve seat, and outlet buffer tank. The side of the buffer tank is connected to the outlet pipe, and the valve rod is connected to the top moving rod. When opened, a throttling section forms between the valve core and the bushing. The diameter of the inlet and outlet pipes is DN200, and the rated stroke of the valve stem is 60 mm.

3.3 Grid Setup

The meshing was done using Fluent Meshing 2020, with the full-size fluid domain obtained based on the solid part. An unstructured hexahedral mesh was used to refine

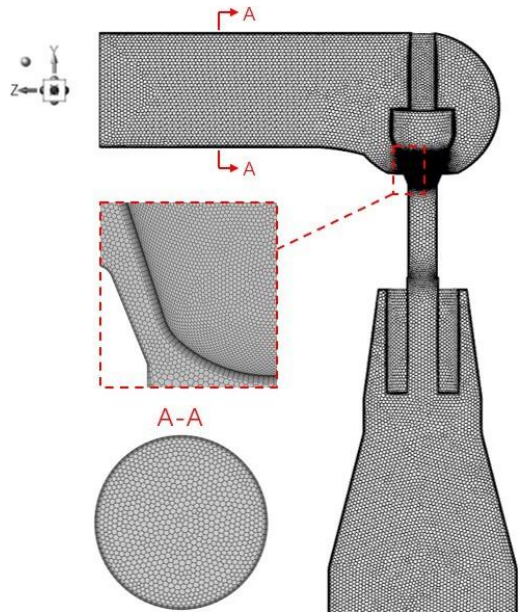

Fig. 2 Meshing distribution

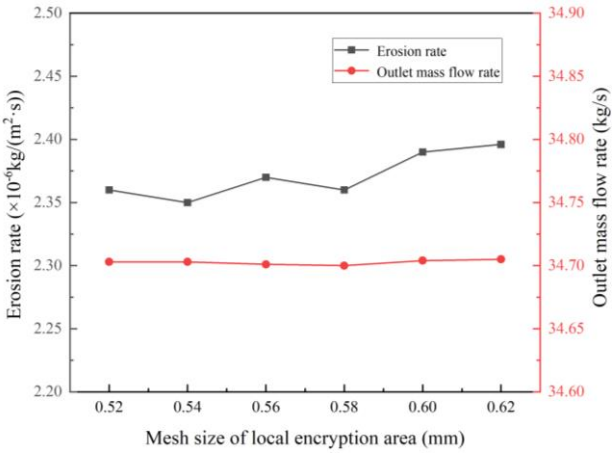

Fig. 3 Validation of grid independence

the mesh in the throttling section, and multi-layer boundary layers was used to capture the turbulence near the wall. Figure 2 shows a vertical section and local enlargement of the control-valve grid division.

To mitigate the impact of mesh resolution on the simulation results, six different resolutions were tested for the throttle section of the valve. Under the same inlet and outlet pressure and 30% opening, the realizable k–ε model and the Oka erosion model were used to analyze the influences of the different mesh resolutions, and the results for valve flow and ER are shown in Fig. 3. Based on these results, we used a grid size of 0.58 mm for subsequent research, corresponding to a total of 1.7 million grid points.

3.4 Boundary Conditions and Solution Method

The internal flow field of the valve was solved for using ANSYS Fluent 2020.R2. The inlet and outlet boundary conditions were pressure inlet and pressure outlet, with liquid water as the flow medium and its compressibility ignored. The turbulence intensity is 5%, and the valve inlet pipeline is extended to ensure the formation of fully developed turbulence at the inlet. This study incorporated the influence of gravity. Based on standard GB/T 17213.2, four models were established with openings of 20%, 30%, 40%, and 50% and corresponding Reynolds numbers of 6.12×10^6, 6.39×10^6, 6.95×10^6, and 7.18×10^6, respectively.

Pressure and velocity coupling was used to solve the problem. The second-order upwind scheme is employed to solve for the turbulent kinetic energy, turbulent dissipation rate, and momentum, and the QUICK algorithm was used to solve for the volume fraction. The flow-field residual was set to 10^{-6}. After obtaining the stable phase-change flow field and ER, the ECDM solution was enabled with a smoothing number of 8 and a variable time step.

3.5 Verification of Erosion Model

To validate the accuracy of the CFD method, a case identical to that of Nguyen et al. (2014) was established. In their experiment, a jet test was conducted using a 6.4-mm nozzle with an inlet velocity of 30 m/s for erosion tests lasting 5 min, 15 min, and 30 min, then the surface depth of the specimens was measured using a three-dimensional surface profilometer. The parameter settings in our simulation were the same as those used by Nguyen et al. in their experiment. Using the ECDM method, simulations were conducted for 300 s, 900 s, and 1800 s, respectively, with Fig. 4(a) showing the experimental setup and Fig. 4(b) showing the curves of erosion depth versus radius. As can be seen, the simulated erosion

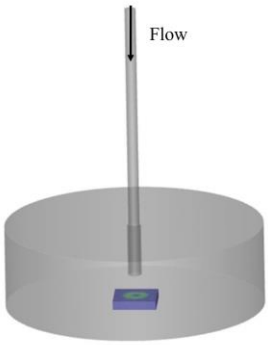

(a) Computational domain

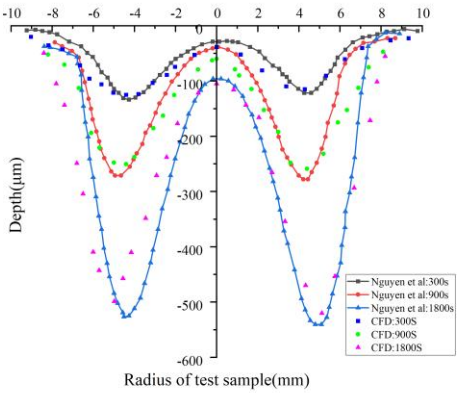

(b) Erosion profile depth comparison along the radius

Fig. 4 Comparison of calculated erosion profiles and experimental measurements by Nguyen et al. (2014)

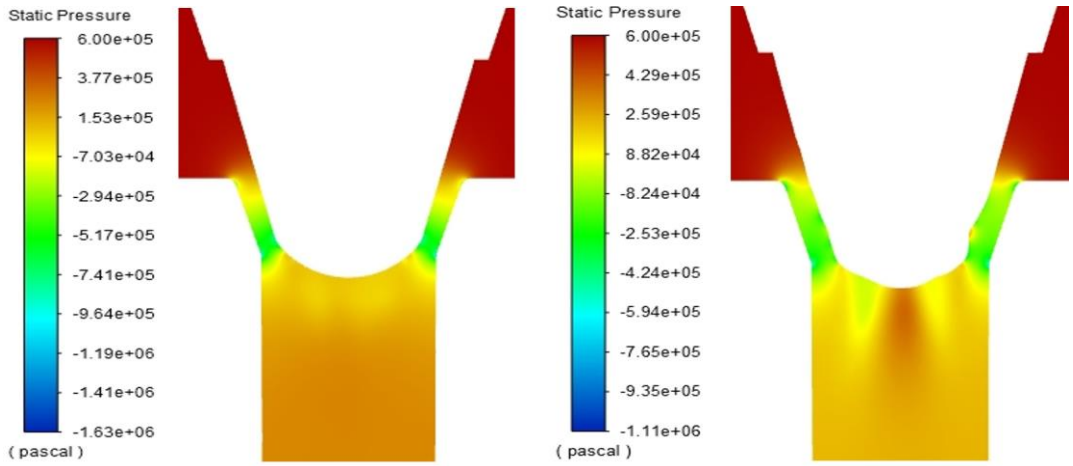

(a) Static mesh (b) Dynamic mesh

Fig. 5 Pressure distribution

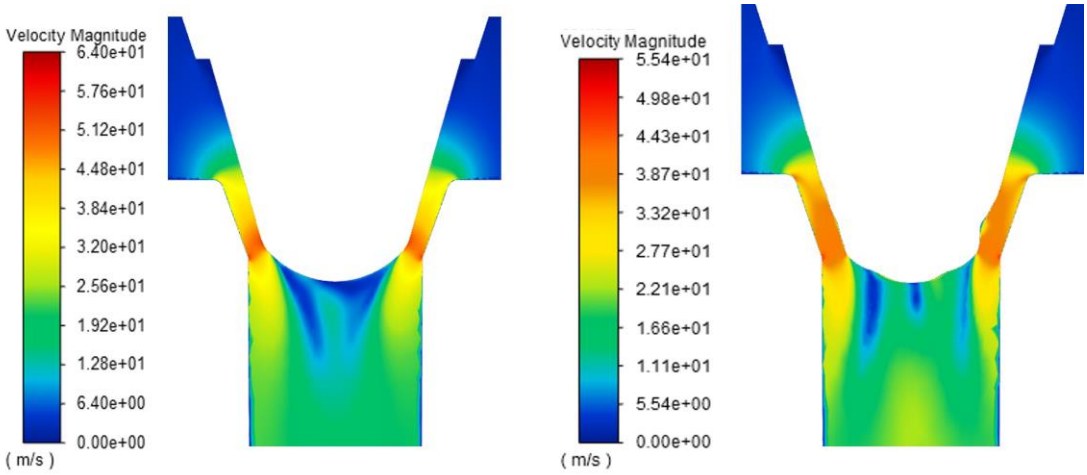

(a) Static mesh (b) Dynamic mesh

Fig. 6 Velocity distribution

morphology and maximum erosion depth are close to the experimental results, showing the reliability of the CFD model and its suitability for subsequent simulation studies.

4. RESULTS AND DISCUSSION

4.1 Analysis of Flow Behavior

Here, we compare the results obtained using a dynamic mesh and a static mesh. Figure 5 shows the comparison for the pressure distribution. The pressure variation in the inlet and outlet pipelines of the valve is relatively minor, with the primary pressure variations occurring in the throttling region. Upon entering the throttling section, the pressure decreases rapidly to below the saturated vapor pressure, resulting in significant pressure fluctuations at the head and surrounding the spool. Figure 5(b) shows clearly that the area with significant surface deformation on the spool coincides with the location exhibiting the most pronounced variations in pressure, and the valve pressure drop calculated using the dynamic grid is smaller. Figure 6 shows the comparison for the velocity distribution. It can be found that the maximum velocity with the dynamic mesh is 8.6 m/s lower than that with the static mesh. When flowing through both sides of the valve core, the velocity with the static mesh increases gradually from 36 m/s to 49 m/s, whereas the velocity with the dynamic mesh is always maintained at ca. 38 m/s.

By monitoring the outlet flow of the valve, it is determined that the flow rate simulated with the dynamic mesh is 2.24 kg/s greater than that with the static mesh. Consequently, it can be inferred that following the erosion of the core, the maximum velocity in the throttling section of the valve decreases, while the average velocity increases. This phenomenon arises primarily from particle erosion, which expands the throttling area and augments the flow area (Zheng et al., 2019), resulting in decreased flow resistance and increased flow rate.

Figure 7 shows the comparison for the vapor-phase volume fraction of the valve longitudinal-sections. To understand the distribution pattern of the vapor-phase more intuitively, a cross-sectional analysis is conducted at the head of the valve spool. The liquid medium undergoes flashing at the valve spool because of the substantial pressure difference, resulting in a significant amount of flash occurring in the lower buffer tank. In Fig. 7(a), the vapor volume fraction is 74.3% at maximum and 11.6% at section A-A. In Fig. 7(b), the vapor volume fraction is 70% at maximum and 4.7% at section B-B. Clearly, the surface deformation of the valve spool affects the flash at the outlet, resulting in a lower overall flash rate.

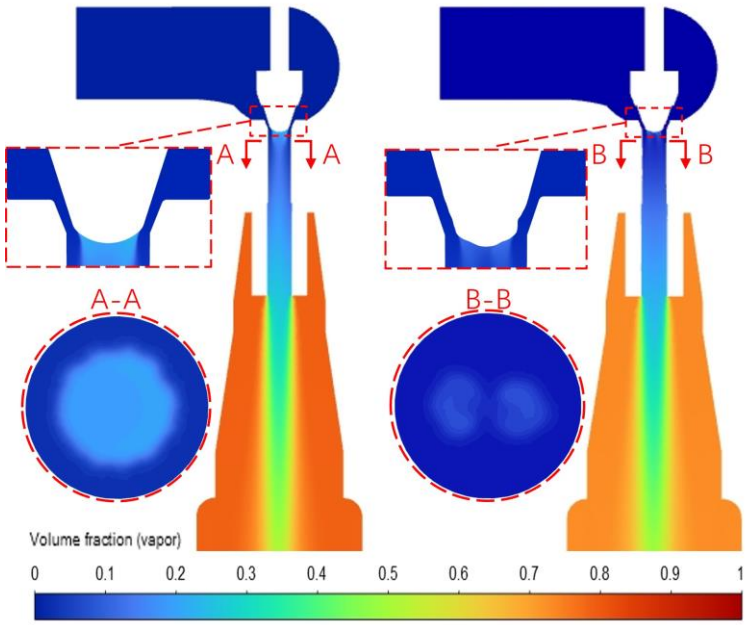

(a) Static mesh (b) Dynamic mesh

Fig. 7 Distribution of vapor volume fraction

4.2 Analysis of Erosion Characteristics

Using a static mesh results in a consistent ER that remains unchanged with time, thereby introducing inaccuracies in the estimation of valve failure. Therefore, the ECDM method offers an improved capability to forecast spool surface deformation and accurately capture particle motion. Figure 8 shows how the ER of the valve core changes with erosion duration for a valve opening of 30%. During an erosion period of 9×10^6 s, the ER decreases with the erosion time, aligning with the result of Zheng et al. (2019). Compared with the ER obtained using a static mesh (represented by the initial data point in Fig. 8), the overall ER decreases by 56.4%. Considering this phenomenon, a further analysis of the erosion parameters is conducted. Figure 9 shows how the maximum particle velocity varies with the erosion time. After a long period of erosion, the throttling area in the valve expands, resulting in a downward trend in the maximum particle velocity.

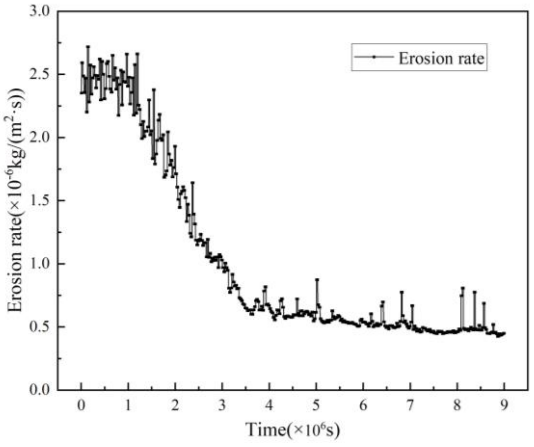

Fig. 8 Variation of erosion rate with time

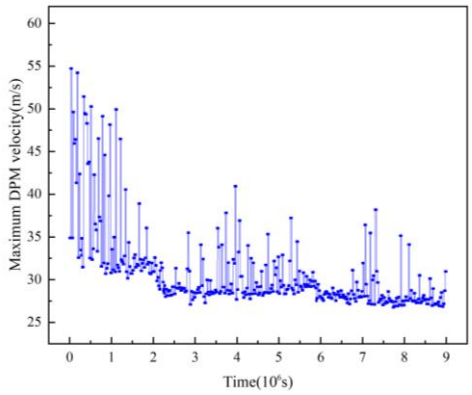

Fig. 9 Variation of maximum particle velocity with time

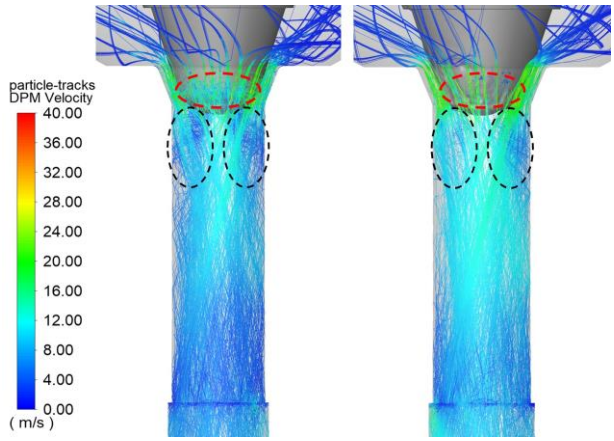

Fig. 10 Comparison of particle trajectories before and after erosion deformation

Figure 10 shows the particle trajectories, with each trajectory colored by particle's velocity. As can be seen, there are two obvious higher-speed vortices at the bottom

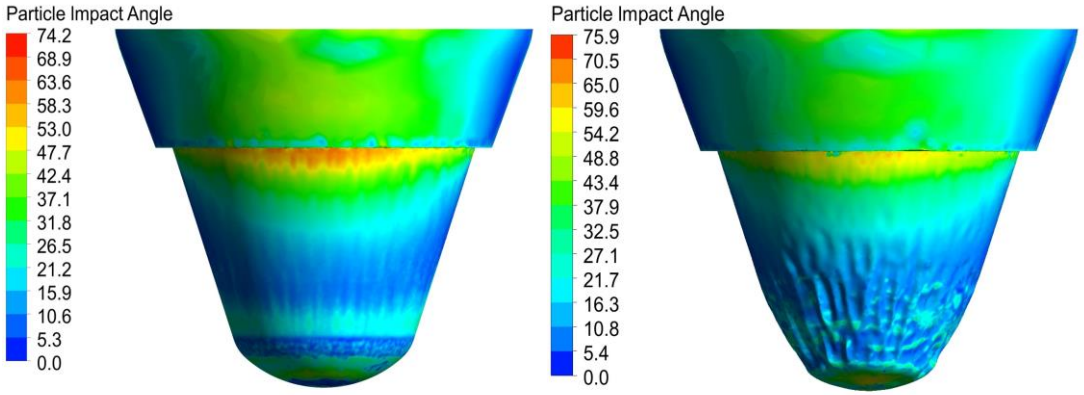

(a) Before erosion deformation (b) After erosion deformation

Fig. 11 Comparison of impact angles before and after erosion deformation

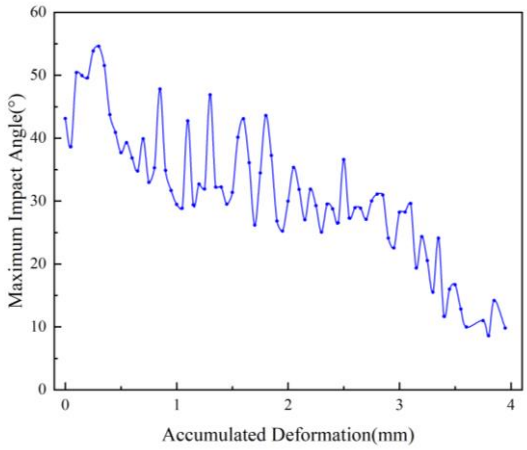

Fig. 12 Maximum impact angle under different surface deformations

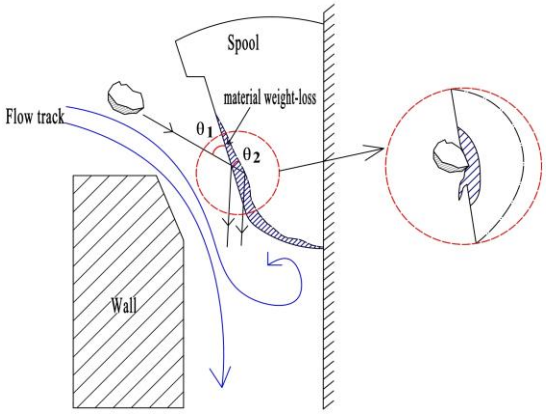

Fig. 13 Schematic of change in law governing particle collision

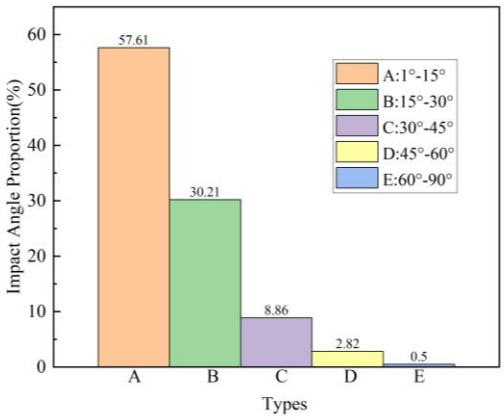

Fig. 14 Proportion of impact angle

of the valve core (see the black dotted areas), and these change the particle trajectories. Prior to erosion deformation, many particles return, resulting in frequent secondary collisions on the valve-core surface and a high collision frequency. Following erosion deformation, the throttling area expands, leading to a reduction in secondary particle collisions and decreased kinetic energy loss (see the red dotted area). Therefore, there are more particles with higher velocity in the outlet bush. Figure 11 shows a comparative analysis of the impact angles of particles on the valve-core surface before and after erosion deformation. During dynamic erosion simulation, the mesh undergoes deformation, leading to changes in the contact angle between the velocity vector of an incident particle and the deformed wall surface (Adedeji & Duarte, 2020). Figure 11 shows that significant changes in erosion angles occur only within the erosion deformation zone of the core head. By extracting post-erosion surface-deformation data from the valve-core head area, the correlation between surface deformation and the maximum impact angle is obtained, as shown in Fig. 12. Clearly, as the erosion deformation of the valve core increases, the particles' impact angles on the wall surface decrease gradually.

Figure 13 provides further insight into this phenomenon, where particles enter the throttling section alongside the fluid medium with an initial impact angle of θ_1. As the valve core undergoes erosion and deformation, the mesh topology shrinks inwardly and deforms, subsequently reducing the impact angle to θ_2.

The alteration of the erosion morphology of the valve core leads to a modification in the collision mechanism governing the interaction between particles and the wall surface. According to the theory of erosion wear, the vertical acceleration of particles at the wall surface induces impacts and cracks, while the tangential acceleration results in cutting and ploughing (Javaheri et al., 2018). Figure 14 shows the distribution of particle impact angles, and analyzing these statistics shows that the

(a) Simulation results with dynamic mesh (b) Actual failure results

Fig. 15 Erosion morphology of valve core

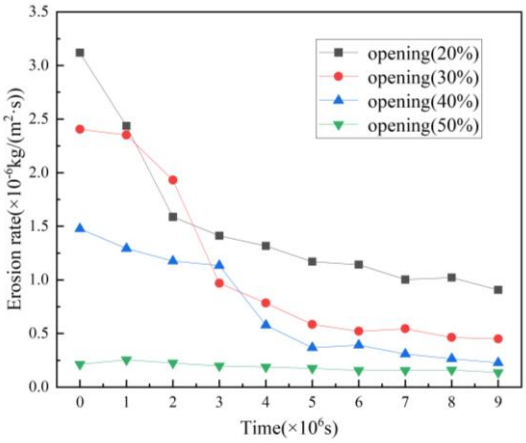

Fig. 16 Changes in erosion rate with time under different openings

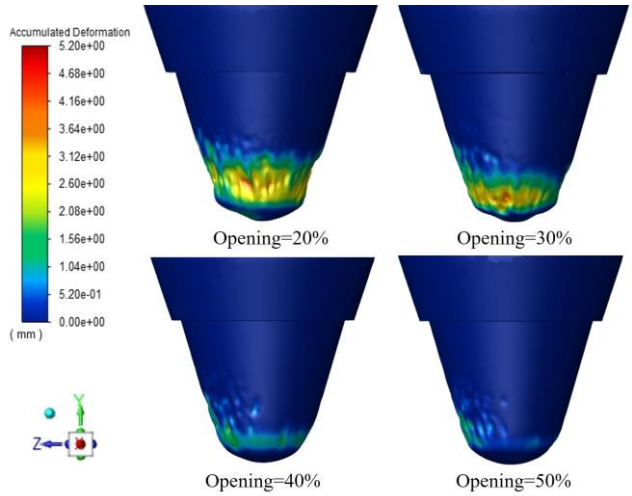

Fig. 17 Erosion deformation of different openings at 9 × 10⁶ s

valve core primarily experiences erosion from particles with small angles (specifically below 30°) during the later stages of operation. Hence, the particles and the wall experience significant effects primarily from cutting and ploughing mechanisms. Figure 15(a) shows the erosion morphology and depth of the valve core obtained from ECDM simulation, while Fig. 15(b) shows the actual failure case of the valve core collected on site. The valve was at 30% opening and the operation time was three months. Both figures exhibit strip erosion morphology, with the erosion area concentrated at the valve core head, and this further confirms the favorable applicability of dynamic erosion simulation.

4.3 Changes of Erosion Law Under Different Opening Degrees

The valve opening was adjusted to 20%, 30%, 40%, and 50%, and the resulting mass flow rate was 32.2 kg/s, 34.7 kg/s, 39.9 kg/s, and 42.1 kg/s, respectively. Figure 16 shows the ER of the valve core with time for the various valve openings. The ER of the valve core varies significantly across the different openings, and comparison shows that it decreases by varying amounts over time. At 20% opening, the ER decreases by 2.21 × 10^{-6} kg/(m^2·s), which is the most. At 40% opening, the ER decreases the fastest, by 84.6% of that at the initial time. The flow characteristics of the control valve do not change linearly, at 50% opening, the flow area of the valve increases noticeably. As a result, the flow suddenly increases, the blockage of fluid weakens, the maximum particle velocity decreases, and wall collisions are greatly reduced, resulting in a significantly decreased ER. This is why the overall ER is relatively small at 50% opening.

Figure 17 shows cloud diagrams of the erosion deformation of the valve core at different openings after an erosion time of 9 × 10^6 s. The region facing the flow (which moves in the −Z direction) is consistently at high risk of erosion. Furthermore, as the opening diminishes, the erosion area extends progressively toward the annular region of the valve-core head. The side facing the flow experiences direct impacts from the majority of particles, resulting in higher collision frequency and greater erosion deformation. Conversely, the opposite side experiences a smaller erosion area and lower ER. This discrepancy arises because the medium must circumvent the valve stem, which significantly diminishes the particles' kinetic energy and subsequently reduces their collision velocity. Simultaneously, it is observed that at 9 × 10^6 s, the erosion deformation diminishes as the spool opening increases, thereby indicating a decrease in the overall ER. This can be ascribed to the augmented opening of the valve core, leading to an expanded throttling area, enhanced fluid flow stability, reduced particle velocity, and diminished interaction between particles and the wall surface.

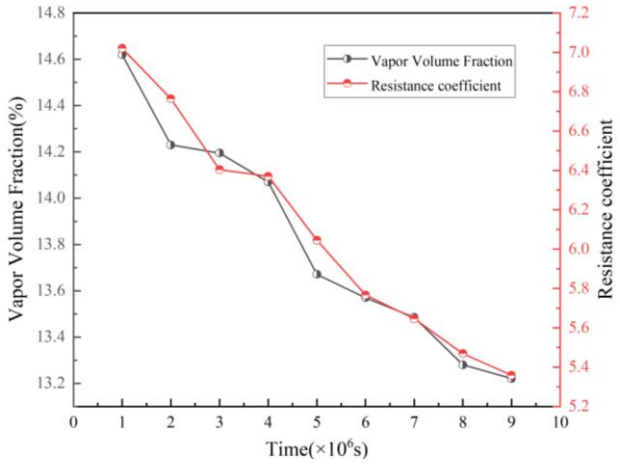

Fig. 18 Changes in vapor volume fraction and flow resistance coefficient with erosion time

4.4 Flash Vaporization Law

Because of prolonged exposure to high differential pressure, the flow channels adjacent to the valve core undergo sudden contraction, resulting in decreased pressure. When the fluid exits the throttling section, the pressure recovers rapidly, but despite this, as the flow persists, the liquid pressure is in places still lower than the saturated vapor pressure. Therefore, to restore equilibrium, the liquid phase absorbs latent heat, leading to flash vaporization. The quantity of flash vaporization is correlated directly with the longevity of the valve. To investigate the connection between flash gasification and flow characteristics within the valve and considering the erosion time, a flow resistance coefficient ξ is introduced. This is determined primarily by the pressure loss and is calculated as:

$$\xi = \frac{2000 \times \Delta p_v}{\rho \times v^2}, \tag{20}$$

where Δp_v [kPa] is the pressure difference between the valve inlet and outlet, ρ [kg/m^3] is the fluid density, and v [m/s] is the fluid velocity.

Through the above analysis, the erosion deformation of the valve spool will cause the pressure change in the valve, and the pressure change will directly affect the flash gasification efficiency (Liao & Lucas, 2015). Figure 18 illustrates the distribution of pressure and vapor volume fraction at the valve outlet under varying erosion durations. It is evident that the pressure loss within the valve diminishes gradually as a result of prolonged erosion, while the fluid density and velocity exhibit minimal changes. Consequently, the flow resistance coefficient demonstrates a declining pattern, leading to a gradual reduction in the amount of flash gasification within the valve.

5. CONCLUSION

Reported herein was a numerical investigation of the erosion failure of a high-differential-pressure control valve in a blackwater flash system. The ECDM method was used to forecast the erosion in the valve, with surface erosion deformation induced by altering the mesh topology. The outcomes obtained with a dynamic mesh and a static mesh were compared, the erosion parameters were analyzed to determine how they vary with erosion time and opening degree, and the flash evaporation occurring in the valve was investigated based on the erosion deformation. The results show the following.

(1) Comparing the results obtained with dynamic and static meshes showed that using a dynamic mesh gives lower maximum flow rate, pressure drop, and flash vapor-phase volume fraction. Over a simulation period of 9 × 10^6 s, the ER with the dynamic mesh decreases by 56.4%, and this reduction can be caused by the fact that erosion induces significant surface deformation on the valve core, resulting in decreased particle velocities, reduced secondary particle collisions, and decreased maximum impact angle. The erosion process primarily involves small-angle particle cutting, accounting for 87.8% of the total.

(2) As the erosion time increases, the ER for each opening diminishes gradually, and the ER of the valve core varies depending on the opening size. The region facing the flow (which moves in the −Z direction) is at higher risk of erosion. As the opening decreases, the erosion area expands progressively toward the annular region of the valve-core head. At 9 × 10^6 s, the erosion deformation decreases as the valve opening increases.

(3) The findings of this study indicate that as erosion time increases, the vapor volume fraction in the valve decreases, accompanied by a decrease in the flow resistance coefficient. These results offer valuable insights for the monitoring of valve conditions.

ACKNOWLEDGEMENTS

This work is supported by the National Natural Science Foundation of China (Grant No.52176048, No. 51876194, No. U1909216). We are grateful for that.

CONFLICT OF INTEREST

No potential conflict of interest was reported by the authors.

AUTHORS CONTRIBUTION

G. F. Ou: Conceptualization, Methodology, Funding acquisition, Project administration; **C. G. Wang**: Writing Original Draft, Visualization, Data Curation; **H. Z. Jin**: Writing Review & Editing, Supervision, Resources, Validation, Investigation; Formal analysis, Data curation.

REFERENCES

Adedeji, O. E., & Duarte, C. A. R. (2020). Prediction of thickness loss in a standard 90° elbow using erosion-coupled dynamic mesh. *Wear, 460-461*. https://doi.org/10.1016/j.wear.2020.203400

Alnak, D. E., Koca, F., & Alnak, Y. (2022). Numerical investigation of the effect of impeller blade angle for

stirred tank. *Sakarya University Journal of Science, 26*(2), 397-409. https://doi.org/10.16984/saufenbilder.992396

ANSYS, ANSYS 2020 R2 Theory Guide (2020). Technical Report. ANSYS Fluent Theory Guide, V. 20.2.

Duarte, C. A. R., De Souza, F. J., Salvo, R. D. V., & Dos Santos, V. F. (2017). The role of inter-particle collisions on elbow erosion. *International Journal of Multiphase Flow, 89*, 1-22. https://doi.org/10.1016/j.ijmultiphaseflow.2016.10.001

Forder, A., Thew, M., & Harrison, D. (1998). A numerical investigation of solid particle erosion experienced within oilfield control valves. *Wear, 216*(2), 184-193. https://doi.org/10.1016/S0043-1648(97)00217-2

Hu, G., Wu, W., Xu, J., & Liao, H. (2022). Research on the erosion performance of a new normally open arrow-type check valve spool. *Journal of Failure Analysis and Prevention, 22*(4), 1725 - 1732. https://doi.org/10.1007/s11668-022-01467-w

Javaheri, V., Porter, D., & Kuokkala, V. T. (2018). Slurry erosion of steel – Review of tests, mechanisms and materials. *Wear, 408-409*, 248-273. https://doi.org/10.1016/j.wear.2018.05.010

Jin, M. S., Ha, C. T., & Park, W. G. (2017). Numerical study on heat transfer effects of cavitating and flashing flows based on homogeneous mixture model. *International Journal of Heat and Mass Transfer, 109*, 1068-1083. https://doi.org/10.1016/j.ijheatmasstransfer.2017.02.080

Koca, F. (2022). Numerical Investigation of corrugated channel with backward-facing step in terms of fluid flow and heat transfer. *Journal of Engineering Thermophysics, 31*, 187-199. https://doi.org/10.1134/s1810232822010143

Koca, F., & Zabun, M. (2021). The effect of outlet location on heat transfer performance in micro pin-fin cooling used for a CPU. *The European Physical Journal Plus, 136*(11). https://doi.org/10.1140/epjp/s13360-021-02113-4

Li, Y., Du, J., Lan, Y., Du, H., & Huang, H. (2022). Numerical analysis of the factors influencing the erosion of the valve port of a high-speed On/Off valve. *Applied Sciences, 12*(12). https://doi.org/10.3390/app12126212

Liao, Y., & Lucas, D. (2015). 3D CFD simulation of flashing flows in a converging-diverging nozzle. *Nuclear Engineering and Design, 292*, 149-163. https://doi.org/10.1016/j.nucengdes.2015.06.015

Liu, E., Li, D., Li, W., Liao, Y., Qiao, W., Liu, W., & Azimi, M. (2021a). Erosion simulation and improvement scheme of separator blowdown system ——A case study of Changning national shale gas demonstration area. *Journal of Natural Gas Science and Engineering, 88*. https://doi.org/10.1016/j.jngse.2021.103856

Liu, X., Ji, H., Liu, F., Li, N., Zhang, J., & Ren, W. (2021b). Particle motion and erosion morphology of the spool orifice in an electro-hydraulic servo valve under a small opening. *Proceedings of the Institution of Mechanical Engineers, Part C: Journal of Mechanical Engineering Science, 236*(6), 3160-3173. https://doi.org/10.1177/09544062211034912

Liu, X. q., Liu, F., Ji, H., Li, N., Wang, C., & Lin, G. (2023). Particle erosion transient process visualization and influencing factors of the hydraulic servo spool valve orifice. *Flow Measurement and Instrumentation, 89*. https://doi.org/10.1016/j.flowmeasinst.2022.102273

López, A., Stickland, M. T., & Dempster, W. M. (2018). CFD study of fluid flow changes with erosion. *Computer Physics Communications, 227*, 27-41. https://doi.org/10.1016/j.cpc.2018.02.002

Morsi, S. A., & Alexander, A. J. (2006). An investigation of particle trajectories in two-phase flow systems. *Journal of Fluid Mechanics, 55*(02). https://doi.org/10.1017/s0022112072001806

Nguyen, V. B., Nguyen, Q. B., Liu, Z. G., Wan, S., Lim, C. Y. H., & Zhang, Y. W. (2014). A combined numerical–experimental study on the effect of surface evolution on the water–sand multiphase flow characteristics and the material erosion behavior. *Wear, 319*(1-2), 96-109. https://doi.org/10.1016/j.wear.2014.07.017

Oka, Y. I., Okamura, K., & Yoshida, T. (2005). Practical estimation of erosion damage caused by solid particle impact. *Wear, 259*(1-6), 95-101. https://doi.org/10.1016/j.wear.2005.01.039

Ou, G., Ouyang, P., Zheng, Z., Jin, H., Bie, K., & Wang, C. (2019). Investigation on failure process and structural improvement of a high-pressure coal water slurry valve. *Engineering Failure Analysis, 96*, 1-17. https://doi.org/10.1016/j.engfailanal.2018.09.003

Parsi, M., Jatale, A., Agrawal, M., & Sharma, P. (2019). Effect of surface deformation on erosion prediction. *Wear, 430-431*, 57-66. https://doi.org/10.1016/j.wear.2019.04.019

Peng, D., Dong, S., Wang, Z., Wang, D., Chen, Y., & Zhang, L. (2021). Characterization of the solid particle erosion of the sealing surface materials of a ball valve. *Metals, 11*(2). https://doi.org/10.3390/met11020263

Thomson, G. W. (1946). The Antoine equation for vapor-pressure data. *Chemical Reviews, 38*(1), 1-39. https://doi.org/10.1021/cr60119a001

Zhao, Y., & Mi, J. (2023). Cavitation characteristics and structure optimization of two-dimensional valve based on entropy production theory. *Journal of*

Applied Fluid Mechanics, 16(9), 1792-1805. https://doi.org/10.47176/JAFM.16.09.1715

Zheng, S., Luo, M., Xu, K., Li, X., Bie, Q., Liu, Y., & Liu, Z. (2019). Case study: Erosion of an axial flow regulating valve in a solid-gas pipe flow. *Wear, 434-435*. https://doi.org/10.1016/j.wear.2019.202952

Zwart, P. J., Gerber, A. G., & Belamri, T. (2004). *A two-phase flow model for predicting cavitation dynamics.* Fifth International Conference on Multiphase Flow, Yokohama, Japan. https://www.researchgate.net/publication/306205415